

Enhanced Cell Capture on Functionalized Graphene Oxide Nanosheets through Oxygen Clustering

Neelkanth M. Bardhan,^{†,‡,§,¶,||} Priyank V. Kumar,^{†,¶,⊗} Zeyang Li,^{||} Hidde L. Ploegh,^{||,⊥,||} Jeffrey C. Grossman,^{*,†} Angela M. Belcher,^{*,†,‡,§} and Guan-Yu Chen^{*,#,∇}

[†]Department of Materials Science and Engineering, Massachusetts Institute of Technology, Cambridge, Massachusetts 02139, United States

[‡]Department of Biological Engineering, Massachusetts Institute of Technology, Cambridge, Massachusetts 02139, United States

[§]The Koch Institute for Integrative Cancer Research, Massachusetts Institute of Technology, Cambridge, Massachusetts 02139, United States

^{||}Whitehead Institute for Biomedical Research, Cambridge, Massachusetts 02139, United States

[⊥]Department of Biology, Massachusetts Institute of Technology, Cambridge, Massachusetts 02139, United States

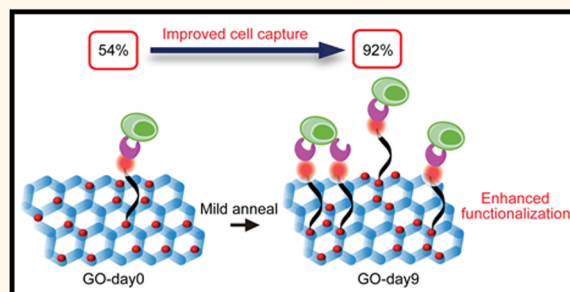
[#]Institute of Biomedical Engineering, National Chiao Tung University, Hsinchu 30010, Taiwan

[∇]Department of Biological Science and Technology, National Chiao Tung University, Hsinchu 30010, Taiwan

S Supporting Information

ABSTRACT: With the global rise in incidence of cancer and infectious diseases, there is a need for the development of techniques to diagnose, treat, and monitor these conditions. The ability to efficiently capture and isolate cells and other biomolecules from peripheral whole blood for downstream analyses is a necessary requirement. Graphene oxide (GO) is an attractive template nanomaterial for such biosensing applications. Favorable properties include its two-dimensional architecture and wide range of functionalization chemistries, offering significant potential to tailor affinity toward aromatic functional groups expressed in biomolecules of interest. However, a limitation of current techniques is that as-synthesized GO nanosheets are used directly in sensing applications, and the benefits of their structural modification on the device performance have remained unexplored. Here, we report a microfluidic-free, sensitive, planar device on treated GO substrates to enable quick and efficient capture of Class-II MHC-positive cells from murine whole blood. We achieve this by using a mild thermal annealing treatment on the GO substrates, which drives a phase transformation through oxygen clustering. Using a combination of experimental observations and MD simulations, we demonstrate that this process leads to improved reactivity and density of functionalization of cell capture agents, resulting in an enhanced cell capture efficiency of $92 \pm 7\%$ at room temperature, almost double the efficiency afforded by devices made using as-synthesized GO ($54 \pm 3\%$). Our work highlights a scalable, cost-effective, general approach to improve the functionalization of GO, which creates diverse opportunities for various next-generation device applications.

KEYWORDS: graphene oxide, thermal annealing, phase transformation, oxygen clustering, improved functionalization, microfluidic-free, enhanced cell capture efficiency



The ability to selectively detect, isolate, and quantify biomolecules such as DNA, proteins, and cells in their native environment is an important ongoing area of research in understanding the physiology of various diseases,¹ for early diagnosis,^{2,3} and monitoring of response to treatment.⁴ Toward this end, nanomaterials are ideal for biosensing applications, owing to their superior optical properties, large surface area-to-volume ratio, and their dimensions which are comparable to those of DNA or proteins.^{5–7} In particular,

carbon-based nanomaterials such as graphene and its derivatives are well-suited for these applications, owing to their planar architecture, coupled with a benzene basal structure, which favors strong interaction with the aromatic functional groups in most biomolecules of interest.

Received: October 16, 2016

Accepted: January 13, 2017

Published: January 13, 2017

Among the various forms of graphene, graphene oxide (GO) is of particular interest as a next-generation biosensing material,^{8–11} due to the following benefits: (a) the ability to solution process this material for large-scale, inexpensive production of thin films,^{12–15} (b) the ease of deposition on a wide variety of substrates, with excellent control over the thickness of the sheets ranging from the micron-scale down to a monolayer,^{14,15} and (c) the availability of methods to fine-tune the sensitivity and selectivity of detection¹¹ through additional approaches involving covalent^{8,16,17} or noncovalent^{18,19} functionalization of the rich carbon and oxygen framework,²⁰ resulting in nanocomposites²¹ with enhanced performance in biomolecule detection.²²

Despite a decade's worth of research activity in the field of GO,²³ nanosheets of GO are still being employed *directly* (in their as-synthesized form) in many applications, and attempts to exercise any control over their physical or chemical structure, with an aim to improve the functionalization density, have been lacking. As a result, device performance is generally boosted by making improvements to the device architecture (through hierarchical designs, such as the use of patterned surfaces in microfluidic chips), rather than taking advantage of the active material itself (in this case, GO). Until now, there have been a few reported examples of the application of GO-based composites for cell-capture: specifically the capture of circulating tumor cells from whole blood,^{24–26} or for antimicrobial surface coatings.²⁷ However, these approaches have relied on functionalization chemistries to conjugate additional cell-capture moieties *directly* on the GO (as-synthesized), or after *reduction* to reduced graphene oxide (rGO). For example, when Yoon *et al.*²⁴ used GO chips directly, they reported low capture efficiency ~40%. Only upon using microfabrication to predeposit “flower-shaped” gold patterns with adsorbed GO were they able to obtain higher efficiency ~73%. Subsequently, Li *et al.*²⁵ reported high sensitivity capture of cells from whole blood, up to ~93% efficient, using rGO films; however, this approach relies on the surface topography and the low stiffness, without trying to specifically improve the conjugation of antibodies on the substrate at the nanoscale level. These approaches suffer from significant limitations which preclude their use in high throughput screening, such as (a) the need to employ expensive fabrication process for large-area devices, owing to the use of gold patterning,²⁴ or (b) the use of antibody-functionalization,^{25,26} which limits the density of capture agents per unit area of device, due to steric effects owing to their size (~150 kDa), and increases the cost of the device due to expensive antibody production techniques, or (c) the requirement to run the assay under controlled environments, such as in 5% CO₂ at 37 °C for long durations ~45 min,²⁵ which may preclude their application in resource-constrained settings. Evidently, such cell capture platforms have relied largely on manipulating the device architecture. To the best of our knowledge, no effort has been made in the literature to improve the fundamental physical and chemical structure of the nanomaterial itself, with the aim to capitalize on the rich carbon–oxygen framework of GO²⁸ to improve the device efficiency.

In this work, we engineer the structure of GO, coupled with the use of nanobodies (single-domain antibodies), to enhance functionalization, and consequently, device performance for biosensing applications. This approach addresses the issues of device scalability, cost and density of cell capture agents discussed above. We utilize a one-step phase transformation process, without any chemical treatments, to control and tune the distribution of oxygen functional groups on the as-

synthesized GO substrates. Further, using a combination of a sortase-mediated transpeptidation reaction along with a “click” coupling reaction, we attach fluorescently labeled nanobodies to the surface of PEG-modified GO substrates. Assembly of this structure into a cell capture device allows efficient, rapid cell capture (10 min.), from small volumes of whole blood (30 μL), under ambient conditions (room temperature incubation, without fractionation of the blood), at almost double the efficiency compared to devices made using as-synthesized GO. This has the potential to develop into a robust, unexplored platform of low-cost diagnostics, for deployment in communities with lack of access to advanced healthcare facilities. To our knowledge, this is the principal demonstration of “phase engineering” in GO, and a showcase of its enormous potential (almost doubling the efficiency of our biosensor). Given that phase engineering has been employed successfully in two-dimensional materials such as transition metal dichalcogenide monolayers to obtain superior device performance,^{29,30} it is imperative to investigate the possibility of using this approach to our benefit in graphene-based devices. Consequently, the technique proposed in this work offers a general method to enhance the functionalization of GO structures, which has broad implications in a range of next-generation devices using GO as a template material.

RESULTS AND DISCUSSION

Phase Transformation in GO. To begin, we discuss a method to control and improve the distribution of oxygen functional groups on the GO nanosheets, using a mild thermal annealing process, without the use of reduction (thermal or chemical) or other chemical treatments. As-synthesized GO structures, with a chemically heterogeneous distribution of oxygen functional groups, are metastable in nature. At mild annealing temperatures (50–80 °C), they undergo a remarkable phase transformation³¹ into distinct oxidized (*sp*³) and graphitic (*sp*²) domains, which is thermodynamically favored and kinetically accelerated by the thermal treatment. Besides, Monte Carlo simulations and recent experiments by several groups have also confirmed^{32–34} that such a phase transformation is favorable at the temperatures mentioned above. Specifically, the oxygen atoms diffuse along the graphene basal plane leading to the formation of distinct graphitic (1–2 nm) and oxygen clusters, as shown in Figure 1a, with the overall oxygen content preserved during this process. We verified this phase transformation process using X-ray photoelectron spectroscopy (XPS) and electrical measurements.

To monitor the structural evolution of GO, we deposited thin films of GO onto clean silicon or glass substrates, and annealed them at 80 °C for a course of 0–9 days. Figure 1b shows the variation in the oxygen concentration, sheet resistance, *sp*² (C=C–C) carbon fraction and the absorbance of thin film samples with annealing time (*t* = 0, 1, 5, or 9 days). Additional XPS data, including the C 1s spectra, as well as the analysis of the C:O ratio and relative fractions of the various functional groups are presented in Figure S4 and Tables S1 and S2 of the [Supporting Information](#). The oxygen concentration is observed to remain constant at ~32–34 atomic percent (at.%) throughout the duration of annealing, consistent with previous reports,^{31–35} which confirms that the phase transformation process results in a redistribution of the oxygen functional groups, without loss in total oxygen content. The process of oxygen diffusion, which results in the clustering of oxygen atoms upon thermal annealing, is discussed in detail in our previous work.³¹ Mechanistically, the process may be attributed to thermodynamic favorability (strain

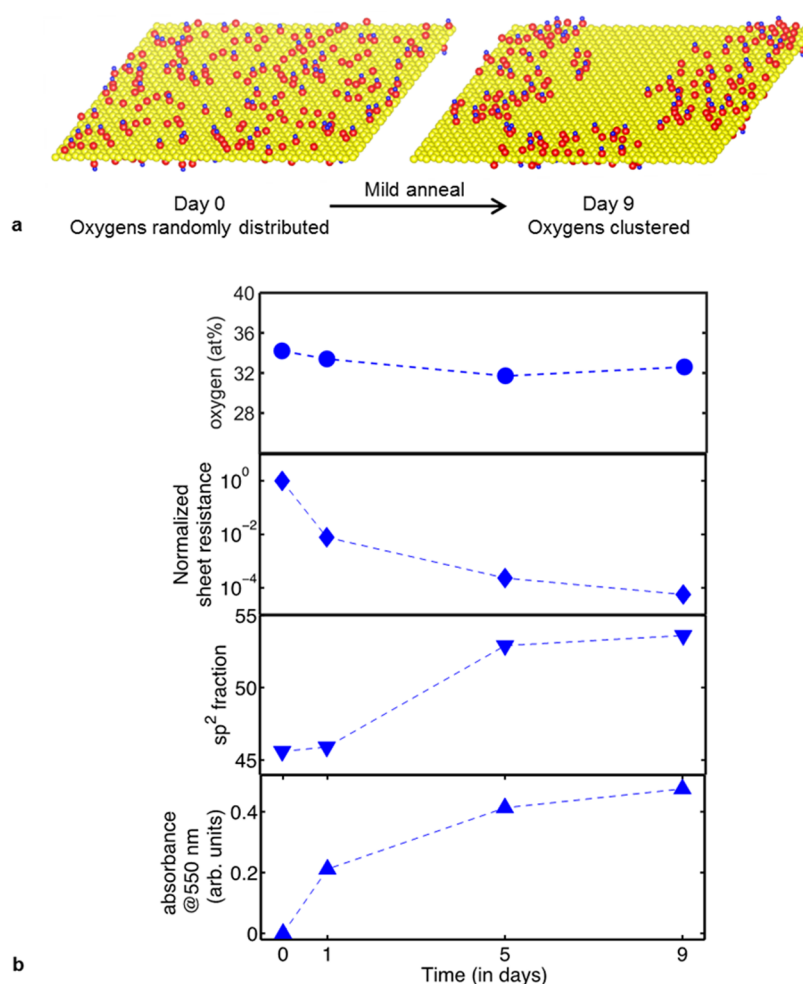


Figure 1. Phase transformation in GO structures. (a) Schematic of the phase transformation process induced in GO structures. Upon mild annealing of as-synthesized GO at 80 °C, the mixed sp^2 – sp^3 phase gradually separates into distinct sp^2 (graphitic) and sp^3 (oxidized) domains, while largely preserving the oxygen content. The yellow spheres represent the carbon atoms forming the graphene basal plane, while the red and blue spheres represent oxygen and hydrogen atoms, respectively. (b) Variation in the oxygen content (at.%), sheet resistance, sp^2 fraction and optical absorbance (at 550 nm) of GO thin films, relative to the properties of as-synthesized GO, measured as a function of the duration of annealing at 80 °C. While the oxygen content remains mostly unchanged, the others show a gradual change with the annealing time, from $t = 0$ (as-synthesized) to 9 days, indicating that GO undergoes a structural change with the oxygen content preserved, consistent with the schematic shown in (a).

relief in the GO structures caused by oxygen clustering, leading to a decrease in the total energy of the system), as well as kinetic acceleration (activation energy for diffusion of oxygen functional groups provided by the mild thermal annealing treatment).

In contrast to the oxygen content, the sheet resistance, the sp^2 fraction and the visible absorbance all show gradual changes over the period of annealing. The sheet resistance decreases by up to four orders-of-magnitude, while the sp^2 fraction increases from ~45% to ~53%, suggesting clustering of sp^2 networks to form distinct graphitic domains, which consequently improves carrier hopping across the graphene plane. In addition, our UV–vis measurements on GO thin film samples showed monotonically increasing absorbance values in the visible, indicating opening up of small optical gaps in GO upon mild annealing (for full spectra, see Figure S1 in the Supporting Information). Since it is well-known^{36,37} that the optical gap is inversely related to the sp^2 cluster size in amorphous carbon systems containing a mixture of sp^2 and sp^3 domains, our result confirms an increase in the sp^2 cluster size with mild annealing. Taken together, these results indicate that while the total oxygen content of GO sheets is largely preserved, the oxygen functional groups on the graphene

basal plane undergo a reorganization, which accounts for the gradual variation in the sheet resistance, the sp^2 fraction and the visible absorbance. This is consistent with the phenomenon as depicted in the schematic shown in Figure 1a. Additional characterizations of the phase transformation process, including direct (Auger electron spectroscopy mapping) and indirect (2D Raman and PL spectra) evidence, as well as FTIR and Raman measurements are discussed in our previous work,³¹ and subsequently been replicated successfully by several other groups of researchers.^{32–34}

Construction of the Cell Capture Device. To investigate the impact of nanoscale phase transformation on cell capture performance, we carried out cell capture experiments on devices using GO nanosheets as a suitable template for functionalization. The device presented here provides a simple platform to capture cell populations efficiently on flat substrates. GO nanosheets were coated onto standard microscope glass slides as substrates, measuring 25 × 75 mm in size, to obtain continuous thin films (see Figures S2 and S3 in the Supporting Information). GO-coated slides were then annealed at 80 °C in a temperature-controlled oven, up to a period of 9 days to facilitate phase

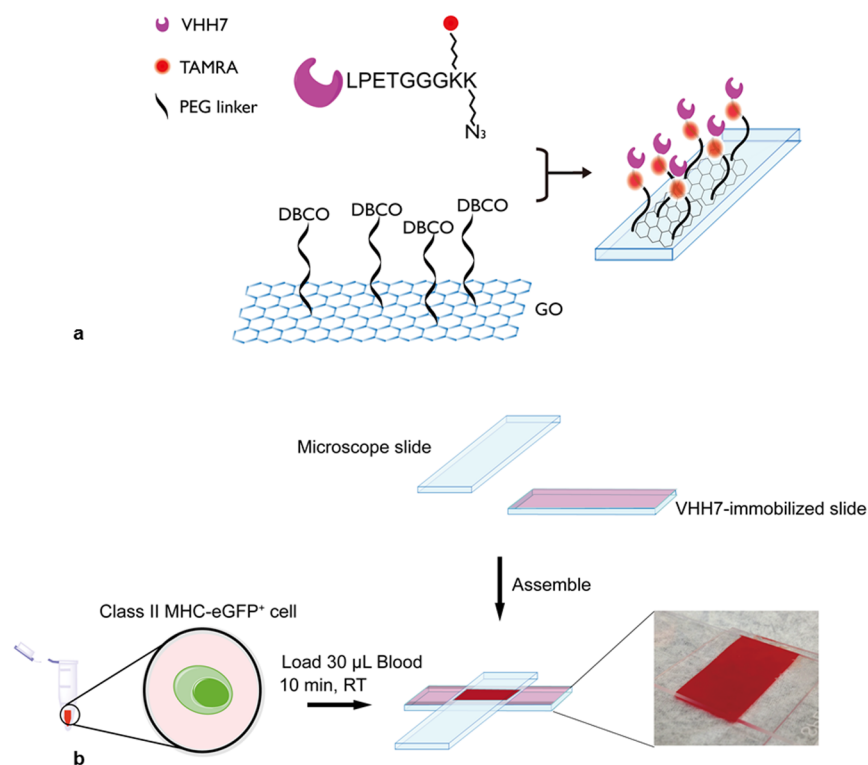


Figure 2. GO functionalization route and cell capture device. (a) Schematic showing the functionalization scheme to graft nanobodies onto the GO thin films. GO nanosheets are coated onto the glass substrate, and subsequently functionalized with diamino-polyethylene glycol (NH_2 -(PEG)₁₂-NH₂) linkers. The other end of the PEG linker is functionalized with an NHS-activated dibenzocyclooctyne (DBCO). The single-domain antibody protein (VHH7), which has been labeled with an azide linker through the LPETGGG motif in a sortase-catalyzed reaction is then “clicked” onto the DBCO in a strain-promoted cycloaddition. (b) Schematic of the cell capture device, with the assay conditions, and a digital color photograph of the loaded capture chamber, constructed to capture cells from murine whole blood.

transformation and oxygen clustering in GO. Slides were retrieved at intervals of 1, 5, and 9 days, to obtain GO samples with varying degree of oxygen clustering, with the day 0 sample showing no clustering, and the day 9 sample showing the greatest degree of clustering. Hereafter, we refer to the day 0 (as-synthesized GO) as the *control* sample, and days 1–9 collectively as the *treated* samples.

We followed a sequential chemical functionalization route to graft nanobodies onto the GO substrates (see Figure 2a for the reaction scheme, as well as Figure S5 in the Supporting Information for a schematic of the functionalization procedure). The GO nanosheets were covalently functionalized with the diamino poly(ethylene glycol) linkers (NH_2 -(PEG)₁₂-NH₂). The free end of the PEG linker was then functionalized with an NHS-activated dibenzocyclooctyne (DBCO). The single-domain antibody fragment (VHH7), which had been labeled with an azide through an LPETGGG peptide motif in a sortase-catalyzed reaction,³⁸ was then “clicked” onto the DBCO in a strain-promoted cycloaddition reaction. VHH7 is a nanobody (heavy-chain-only single-domain antibody), specific for murine class II MHC-positive cells from mouse whole blood. An added advantage of using nanobodies compared to conventional antibodies is their smaller size (~15–20 kDa, compared to ~150 kDa for the latter), expected to result in a higher functionalization density, leading to enhanced cell capture.

The VHH7-GO functionalized slide was assembled with a second glass slide to form a cell capture chamber (Figure 2b). Two strips of double-sided tape served as spacers to yield a chamber of 12 × 25 × 0.1 mm, for a total volume of 30 μ L. The VHH7 is thus directly attached to one of the surfaces of the

capture chamber. Assembly of this device requires no more than two-sided tape and a second, uncoated glass slide. Delivery of 30 μ L of whole blood, or a spiked cell suspension is then achieved³⁹ by contacting the opening of the chamber with the tip of a mechanical pipetting device. Within seconds, discharge of the intended volume then fills the chamber by capillary action. After incubating the sample in the chamber for 10 min, wash steps are conducted in a similar fashion by the delivery of PBS buffer to one open side of the chamber, and wicking off buffer at the opposite end of the chamber, using filter paper to ensure flow across the chamber surfaces. The mechanism of the capture of cells from whole blood is shown in the schematic in Figure S6 in the Supporting Information.

This approach is elegantly adaptable for it to be used in less affluent communities, and could enable a sophisticated platform of low-cost diagnostics (a single cell-capture device based on our *treated*-GO platform works out to be under \$5, see Table S3 in the Supporting Information for an estimation of the cost).

Cell Capture Experiments. As a start, we verified individually the contribution of GO nanosheets and VHH7 nanobodies in the cell capture device, using a mouse B-cell lymphoma (A20) cell line. The cells were spiked in PBS to obtain a cell loading 2×10^5 cells per 30 μ L, and loaded into the device for 10 min at room temperature (see Methods). After the cell capture, the cells were stained with Alexa Fluor 488-labeled anti-murine class II MHC antibody, for fluorescence microscopy. We observed negligible cell capture (or nanobody grafting) in the case of the substrates prepared without VHH7 (or GO nanosheets) respectively (see Figures S7 and S8 of the Supporting Information). These decoupled observations indicate that both

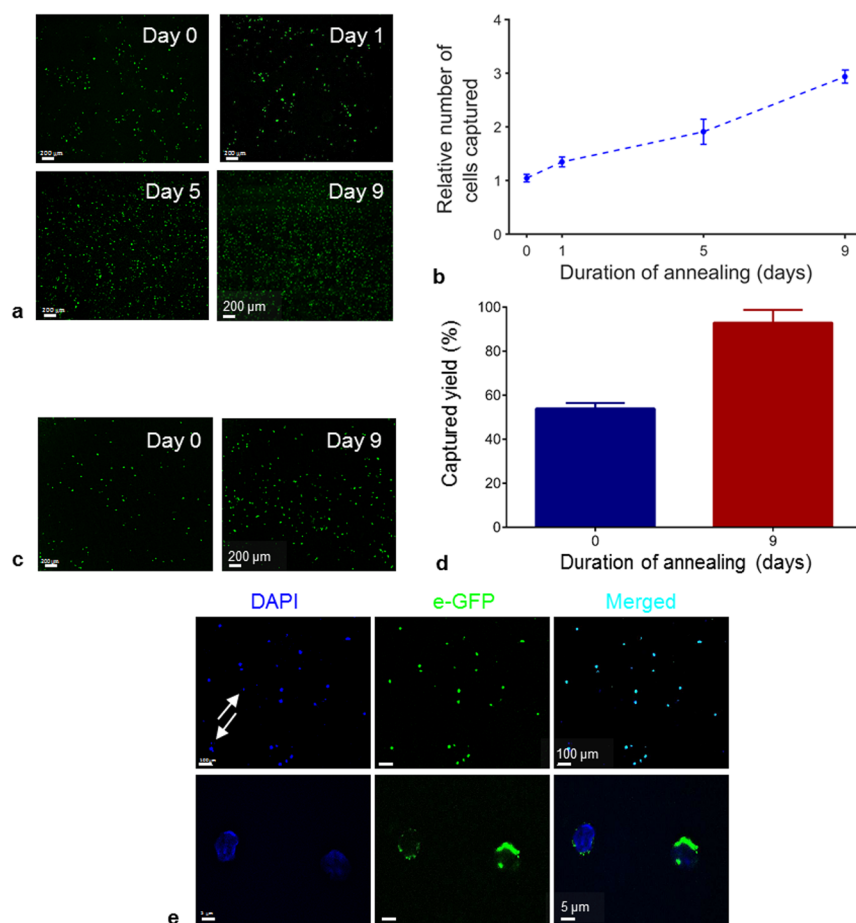


Figure 3. Enhanced cell capture using nanobody functionalization on *treated-GO* substrates. (a) Quantification of captured A20 cells (from cells spiked in PBS) on the *control-* (day 0) and *treated-GO* (day 1–9) substrates. The cells are stained with an Alexa 488-labeled anti-Class II MHC antibody. Scale bar is 200 μm for all images. (b) The relative cell capture efficiencies, for the assay corresponding to (a). Clearly, the number of cells captured increases with the duration of the mild annealing treatment. (c) Quantification of captured class II MHC-positive eGFP⁺ cells from murine whole blood samples, on devices made using *control-* (day 0) and *treated-GO* (day 9) substrates. Scale bar is 200 μm for all images in (a) and (c). (d) The relative capture yield, for the assay corresponding to (c), reveals an almost double cell capture efficiency ($92 \pm 7\%$) for the *treated-GO*, compared to the as-synthesized *control-GO* case ($54 \pm 3\%$). The error bars in (b) and (d) represent the standard deviation of triplicates. (e) (Top panel) Captured cells on the day 9 *treated-GO* substrates were stained with DAPI (blue) and compared with the green fluorescence of the eGFP⁺ MHC-positive cells. The merged image shows excellent colocalization, with very little nonspecific binding, indicated by the presence of DAPI⁺/eGFP⁻ signal (white arrows). (Bottom panel) High resolution images reveal that the captured cells emit green fluorescence on the cell surface, further confirming that they are indeed class II MHC-positive eGFP⁺ cells. Scale bar is 100 μm for the top panel and 5 μm for the bottom panel images.

GO nanosheets and the VHH7 nanobodies play essential roles, respectively—as a template for nanobody grafting, and as a capture agent for specific binding of cells.

We then tested the cell capture performance of VHH7-functionalized *treated-GO* substrates, and compared it with the *control* case, using the same A20 cell line, for two cases: (i) cells spiked in PBS, and (ii) cells from fresh murine whole blood. Figure 3a,b present results from the spiked *in vitro* assay, while Figure 3c–e show the results for cell capture from whole blood.

For the cell capture experiments from cells spiked in PBS, Figure 3a shows a series of fluorescence images comparing captured cells for the *control-* and *treated-GO* cases. Interestingly, in the case of *treated-GO* substrates, we observe monotonically increasing cell capture efficiencies with increasing duration of annealing (day 1–9), evident from the images by a greater degree of the density of fluorescence of the captured cells. Normalized relative to the *control-GO* case, our analysis (Figure 3b) shows a ~ 2 – $3\times$ increase in the number of cells captured by the devices

made using *treated-GO* substrates. These results hold promise for further improving the device performance to achieve significantly higher cell capture efficiency, by using the one-step, mild thermal annealing process for the GO substrate.

Following this, we tested the performance of VHH7-functionalized *treated-GO* substrates, in their ability to capture cells from fresh whole blood samples (Figure 3c–e). Fresh whole blood was obtained from Class II MHC-eGFP knock-in mice, for ready visualization of MHC⁺-cells by their green fluorescence. The cell concentration was estimated to be 15,000 cells per 30 μL . From the fluorescence images in Figure 3c, we observe significantly higher degree of cell capture on devices made from day 9 *treated-GO* substrates, compared to the devices based on day 0 *control-GO*. From image analysis, we report (Figure 3d) an average capture efficiency of $\sim 54 \pm 3\%$ on the VHH7-functionalized nanosubstrate for the day 0 case. In contrast, the cell capture efficiency is increased to $\sim 92 \pm 7\%$ for the day 9 *treated-GO* case, indicating an almost double improvement in performance over the as-synthesized GO substrates.

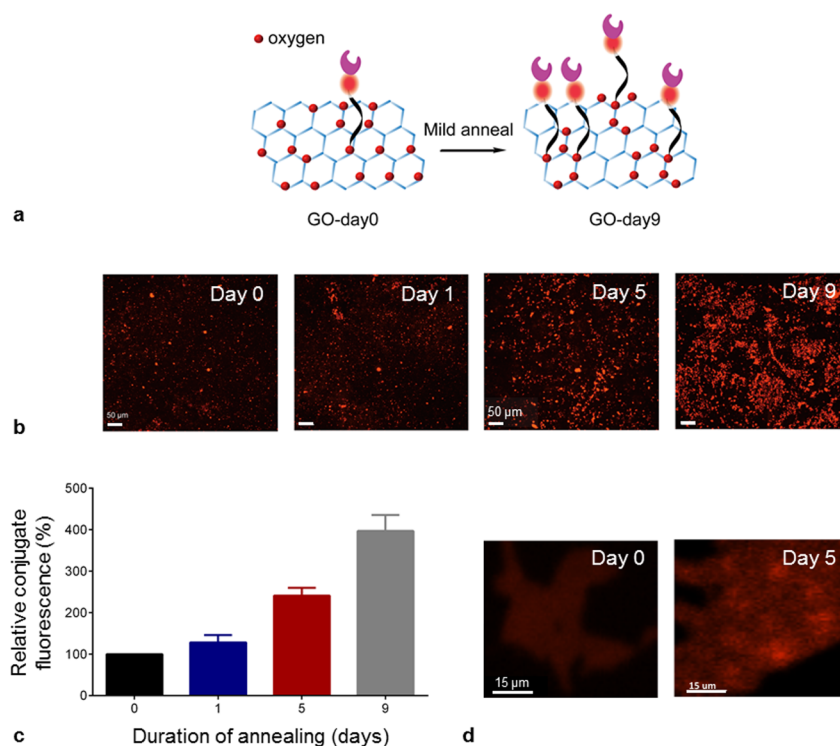


Figure 4. Improved nanobody grafting and linker concentration on *treated*-GO substrates. (a) Schematic of the surface chemistry redistribution caused by the oxygen clustering process, resulting in improved linker- and nanobody-functionalization on *treated*-GO substrates, compared to the *control* (as-synthesized) sample. (b) Fluorescence microscope images, revealing increasing density of nanobodies conjugated on the GO substrates, with increasing duration of annealing. The antibodies are labeled with a TAMRA fluorophore, which is responsible for the red fluorescence. Scale bar is 50 μm for all images. (c) The relative conjugate fluorescence, for the microscope images corresponding to (b), showing up to $\sim 4\times$ increase in the density of functionalization with annealing time, from $t = 0$ to 9 days. The error bars represent the standard deviation of triplicates. (d) Fluorescence microscope images of TAMRA-conjugated linker (without the presence of the nanobody), on the *control* (day 0) and *treated*-GO (day 5) substrates, proving that the increased concentration of the linker functionalization in the *treated*-GO results from the phase transformation process (see also Figure S11 in the [Supporting Information](#)). Scale bar is 15 μm for both images.

It is worth highlighting that these experiments were carried out at room temperature, under ambient conditions, while achieving an efficiency of $\sim 92\%$. This is important for several reasons. Our method avoids the use of an incubator to maintain the temperature at 37 $^{\circ}\text{C}$, without the need for separation of the serum components prior to cell capture. Combined with the use of a simple device architecture (using only two glass slides and double-sided tape, without the need for expensive lithography patterning or microfluidic-based geometries), scalable materials processing on large-area substrates, and relatively inexpensive nanobodies as cell capture agents, this approach facilitates device fabrication and cell capture to be used in remote communities, and in less affluent regions, with lack of access to advanced healthcare facilities.

We performed additional characterization of the captured cells, using confocal microscopy, to determine specificity. All cells captured on the devices were stained using DAPI, in order to evaluate selectivity of our device toward Class II MHC-positive cells. Since DAPI is a nuclear stain, it stains all captured cells equally, thus enabling comparison with the green fluorescence signal expected from the eGFP⁺ MHC-positive cells, to identify nonspecific binding events. Figure 3e (top panel) shows very low quantities of nonspecific binding (for example, due to T-cells), as indicated by the white arrows, corresponding to a DAPI⁺/eGFP⁻ signal. This suggests that the phase transformation process used in our approach to increase the capture efficiency does not result in undesirable characteristics such as nonspecific binding. Further, high-resolution images in the bottom panel of Figure 3e

reveal that the green fluorescence is localized to the cell surface, confirming that they are indeed class-II MHC-positive cells. The captured cells are viable, and available for further staining and analysis.

As a second, independent confirmation of the specificity of cell capture, we repeated the experiment with VHH4 nanobodies conjugated on to the GO substrates, instead of VHH7 (see Figure S10 of the [Supporting Information](#)). Given that VHH4 nanobodies are specific to human Class-II MHC, the lack of appreciable cell capture detected from murine whole blood samples demonstrates the excellent specificity of our cell capture platform.

Mechanism of Enhanced Cell Capture Due to Oxygen Clustering. We hypothesized that the observed enhancement in cell capture is a result of improved antibody grafting, facilitated by improved functionalization of the *treated*-GO nanosheets (see schematic in Figure 4a). We verified this hypothesis by assessing the concentration of nanobodies bound to the GO substrates. By engineering a sortase-ready version of the VHH7 with an LPETG motif near the C-terminus, and using standard sortagging protocols,³⁸ we introduced a Gly peptide equipped with a TAMRA fluorophore and an azide linker to partner with the DBCO moiety during the click reaction, for direct visualization of the conjugated linker through fluorescence imaging.

Figure 4b shows a series of fluorescence images comparing the nanobody-functionalized *control*- and *treated*-GO samples. The results exhibit a monotonous increase in the fluorescence intensity and distribution from day 0 to day 9 samples, indicating

greater concentration of antibody grafting onto the GO substrates that have undergone phase transformation. Specifically, we find an increase in the conjugate fluorescence by $\sim 4\times$ in the day 9 *treated*-GO case, compared to the day 0 *control*-GO (Figure 4c), thereby confirming that the enhanced cell capture is a direct result of improved attachment of nanobodies on the GO substrates.

Further, in order to decouple the effects of antibodies on enhanced cell capture, and to directly probe the concentration of linkers on the surface, we performed an experiment as described above, albeit without VHH7. In this case, the TAMRA fluorophore was conjugated directly to the diamine-PEG linker attached to the GO substrate. The fluorescence images obtained from this experiment for the *control* and *treated* samples (day 5 case) are shown in Figure 4d. These images reveal a clear increase in the fluorescence for the latter case, indicating a greater concentration of linkers on the *treated*-GO substrates. We continued the annealing process for a longer period. Samples annealed for 9, 12, and 15 days showed saturation in the TAMRA fluorescence intensity (see Figure S11 in the Supporting Information for the full set of images). This suggests that a steady-state is attained^{31,32} at a time point between day 9 and day 12, and a corresponding limit is reached in the maximum density of linkers that can be grafted on to the GO substrate. These results imply that improved nanobody grafting onto the GO substrates is a direct consequence of the enhanced functionalization density of the linkers, which itself is a result of the phase transformation process effectuated in the *treated*-GO samples.

Molecular Dynamics (MD) Simulations. In order to understand the reasons behind improved functionalization of GO nanosheets with NH_2 -terminated linkers, we carried out classical MD simulations based on reactive force fields (ReaxFF). The simulations were designed to investigate changes in the surface chemistry that could lead to improved reactivity of the GO structures upon mild annealing. We recall that the difference between the *control*- (as-synthesized, day 0) and *treated*-GO (day 1, 5 and 9) structures lies in the arrangement of the oxygen functional groups (Figure 1a). In the former, the oxygen functionalities are randomly distributed across the graphene plane, while in the latter, the oxygen groups diffuse and form distinct clusters. Although we know that such a process is energetically favorable from our previous work^{31,40} and other literature,^{35,41,42} what exactly happens to the surface chemistry upon clustering, *i.e.*, changes in the relative concentration of oxygen functional groups, remains unknown to date. In what follows, we use MD simulations to shed light on the changes in the surface chemistry of the functional groups on the GO nanosheets, and correlate these results to the changes in the surface reactivity, which is crucial to understanding the improved linker functionalization observed in our experiments.

Model GO structures with different sizes of oxidized and graphitic domains (0, 3, and 6 graphene rows) were prepared (Figure 5a) keeping the oxygen concentration fixed, in order to mimic the phase separation process (as depicted in the schematic in Figure 1a). Initially, the oxidized domains consisted of randomly distributed epoxy and hydroxyl groups attached to both sides of the graphene sheet, consistent with previous reports^{14,43} showing the dominant presence of such functional groups in GO. To account for local variations in the oxygen concentration and fraction of functional groups on the GO sheet, we studied oxygen concentrations (in at.% hereafter) of 10 and 20% in the initial GO structures, and prepared samples with epoxy to hydroxyl

ratios^{44,45} of 3:2 and 2:3. GO structures were then annealed at 300 K using MD simulations (see Methods for details).

Upon equilibration, our MD simulations lead to the formation of realistic, disordered GO structures with distinct graphitic and oxidized domains, containing a mixture of epoxy, hydroxyl and carbonyl functional groups, with a small amount of water molecules, consistent with previous literature.⁴⁶ The generation of 10 samples for each composition allows us to present meaningful ensemble averages of the computed properties. Figure 5b shows the relative functional group distribution of the phase-transformed GO structures generated from our MD simulations. Interestingly, we observe that upon annealing, the relative fraction of the carbonyl functional group increases at the expense of the epoxies and hydroxyls, with increasing oxygen clustering. Specifically, in the case of epoxy-rich GO structures (3:2) at higher oxygen concentration (20%), the relative fraction of the carbonyl functional group nearly doubles upon phase separation.

These results are further corroborated by O 1s XPS spectra collected on our *control*- (as-synthesized) and *treated*-GO samples (Figure 5c). In addition to the presence of the C–O peak at 532.5 eV in the *control* sample, we find the appearance of a distinct peak at 531 eV in *treated*-GO (day 5) sample, which is attributed⁴⁴ to the oxygen forming double bonds with the carbon atom (C=O). This observation suggests that carbonyl formation is consistent with our MD simulations, which explains the role of oxygen clustering in improving the reactivity toward functional linkers, as described below. Additional details about XPS analysis of the functionalized GO substrates, for both *control*- and *treated*-GO samples, are provided in the Supporting Information. Figure S4 shows the C 1s spectra, while Table S1 lists the relative fractions of the carbon and oxygen components. We observe no significant loss in the oxygen content upon thermal annealing, in contrast to thermal or chemical reduction of GO to rGO, indicating a mere redistribution of the oxygen functional groups caused by oxygen clustering during the phase transformation process. This is supported by the data presented in Table S2, which estimates the relative fractions of the various forms of carbon bonds. The ratio of sp^2 -bonded carbon (C=C–C) increases, as well as the amount of carbon forming carbonyl functional groups, at the expense of the epoxies (C–O–C). Further, our MD results are also in agreement with DFT computations by Sun *et al.*, who showed⁴⁷ the formation of carbonyls and lactones to be energetically favored when epoxy groups are present in close proximity.

It is important to note that such rearrangements have been reported previously^{44,48} only when GO nanosheets are subjected to high temperature thermal reduction, where the application of substantial thermal energy drives carbonyl formation, along with oxygen removal. In contrast, our results suggest that the redistribution of the functional groups, and hence the surface chemistry, is strongly affected by a simple process of oxygen clustering on the graphene basal plane induced by our mild thermal annealing treatment, with the overall oxygen concentration remaining constant.

Given our MD results, we proceed toward understanding the role of changing the surface chemistry through oxygen clustering on enhancing the reactivity of GO nanosheets to amine (NH_2) linkers. Our results clearly show that carbonyl groups are generated at the expense of the epoxy groups that are initially present in majority in the GO structures. It is well-known that the carbonyl bond is inherently more reactive⁴⁹ toward nucleophiles (such as R–NH_2) in mild acidic conditions,⁵⁰ compared to epoxy or hydroxyl groups. This is because the carbocation intermediate

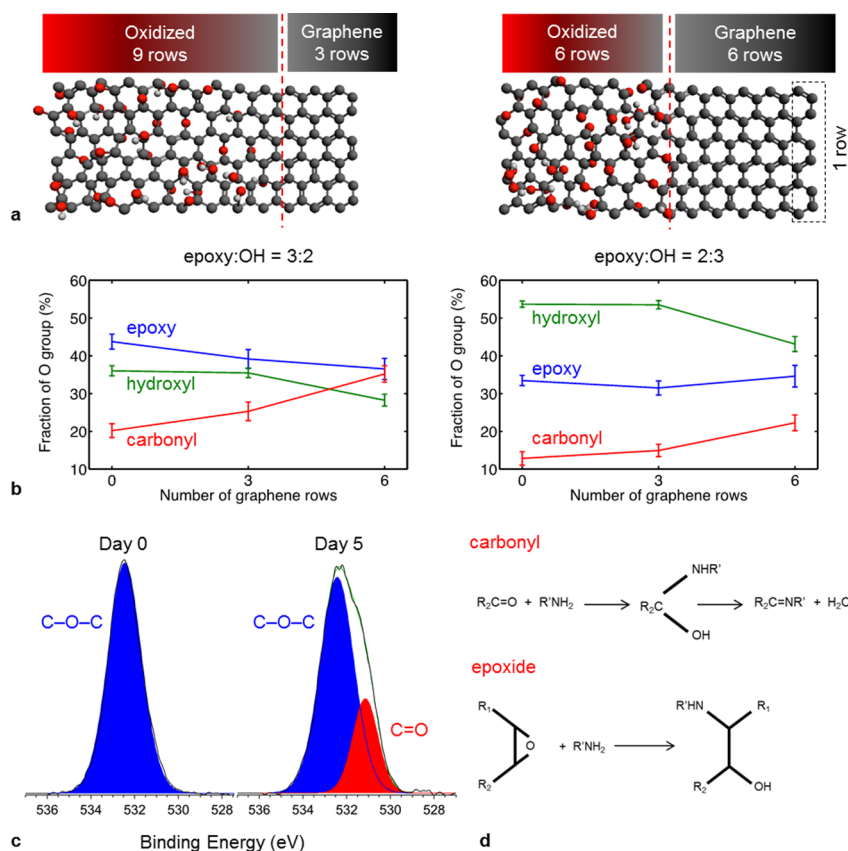


Figure 5. Molecular Dynamics explains the mechanism behind improved functionalization. (a) Representative model GO structures used in MD simulations, to study the impact of oxygen clustering on the chemical group distribution, and subsequent reactivity of the GO structures. Each structure consists of two distinct oxidized and graphene regions with different domain sizes, or “rows”, mimicking different degrees of oxygen clustering. Carbon, oxygen and hydrogen atoms are represented as gray, red and white spheres, respectively. (b) The relative distribution of the functional groups, at different degrees of oxygen clustering (0, 3, and 6 graphene rows) shown in (a), for GO structures with different initial epoxy: hydroxyl ratios of 3:2 (left) and 2:3 (right). The oxygen concentration is chosen to be 20 at. %. (c) O 1s XPS spectra collected on control (day 0) and treated-GO (day 5) samples, showing the appearance of a distinct peak at 531 eV in the latter, attributed to the oxygen double bonds forming with the carbon atom (C=O), at the expense of the epoxy functional groups. (d) Nucleophilic attack by primary amines on the different functional groups in GO, suggesting enhanced reactivity of the enriched carbonyl species toward linker functionalization.

formed in the case of a carbonyl group is strongly stabilized by the resonance electron donation from the bonded oxygen atom, thereby lowering the energy of the transition state significantly. As a result, the nucleophilic addition/elimination reaction is kinetically favored and proceeds faster, leading to the formation of imines (with a C=N group, Figure 5d), which have been reported to be observed^{12,51,52} in the context of GO functionalization. Thus, we infer that the generation of carbonyls in favor of the epoxy groups increases the reactivity of the GO nanosheets toward amine linkers, resulting in improved functionalization.

CONCLUSIONS

In summary, we have developed a method to enhance the ability to efficiently capture cells from whole blood, using graphene oxide nanosheets coupled with nanobodies, by engineering the structure and chemistry of graphene oxide, rather than modifying the device architecture. As a result, our GO-based cell capture devices offer distinct advantages, of being (a) high efficiency, compared to devices based directly on as-synthesized GO, as a result of increased density of functionalization of the linkers for attaching nanobodies, and extremely good specificity of cell capture; (b) easy to manufacture, with a planar architecture, using only two glass slides and double-sided tape, without the use of complex lithographic patterning such as those used in

microfluidic devices; (c) scalable and applicable to large area devices through the mild thermal annealing treatment; (d) inexpensive, due to the use of nanobodies, which can be easily expressed and grown in large-scale at high yield in bioreactors, compared to full-sized antibodies; and (e) highly rapid, ambient-conditions cell capture assay, without the need for incubators or refrigeration equipment, which makes it possible to be deployed in Point-of-Care testing and in areas with lack of access to advanced healthcare facilities.

In particular, compared with other reported immunoaffinity-based cell capture technologies based on as-synthesized or reduced GO substrates, we have demonstrated a planar, highly sensitive device using our treated-GO with an efficiency of ~92% for the capture of Class II MHC-positive cells from murine whole blood at room temperature, which is almost double the efficiency offered by devices made directly using as-synthesized GO. Using MD simulations coupled with experiments, we show that the enhanced efficiency stems from improved reactivity and functionalization of GO structures with linkers and nanobodies, as a result of chemical changes induced by oxygen clustering during the phase transformation in GO. Since the functionalization of GO nanosheets plays a central role in a variety of other applications including catalysis, batteries, solar energy conversion, supercapacitors and chemical sensors, to name a few,

it is worth noting that the methods and analyses presented in this work can be applied broadly to improve the device performance in such applications. These results open up exciting opportunities for tuning the functionalization of as-synthesized GO structures through oxygen clustering, and highlight methods for pushing the efficiency limits of next-generation GO-based devices.

METHODS

GO Thin-Film Preparation and Characterization. GO solutions (4 mg/mL, in water) were purchased (SKU #777676, Sigma-Aldrich, MO, USA). GO coating on clean glass substrates was carried out as follows. To begin, the substrates were coated with 3-aminopropyltriethoxysilane (APTES). GO suspension was immobilized on APTES-functionalized glass through dip coating, by means of electrostatic forces of attraction between the oxide groups of GO and the amine end-terminus of APTES. After coating the substrates for 1 h, the samples were air-dried and then annealed in an oven at 80 °C for $t = 0$ (as-synthesized, or *control*), 1, 5, and 9 days (*treated*), along with an uncoated glass substrate sample (which served as a blank control for our absorbance measurements). For the sake of XPS and electrical measurements, we prepared GO thin films on clean silicon substrates by drop-casting 100 μL of GO solution, resulting in ~ 2 μm -thick and ~ 1 cm-wide (in diameter) films.

UV-vis measurements of GO films on glass were taken using a Cary 500i dual-beam spectrophotometer. The scan range was 300–800 nm at a rate of 600 nm/min, and an integration time of 0.1 s with a step size of 1 nm. A dual beam source was used, with a source changeover at 350 nm, which corresponds to the step seen in the plots in Figure S1 of the Supporting Information. The absorbance data was plotted with a zero baseline correction corresponding to a blank (uncoated) glass substrate. Electrical transport measurements of GO thin films on silicon were carried out using a four-point probe technique (Model 2525, The Micro-manipulator Company, NV, USA) at room temperature. Measurements were taken by varying the applied voltage from -1 to $+1$ V. XPS measurements were taken using a PHI VersaProbe II Scanning XPS microprobe (Physical Electronics Inc., MN, USA). An Al K α source was used, with an incident X-ray photon energy of 1,486.7 eV. The spot size was 200 μm , with a sample tilt of 45° and a hemispherical analyzer with a pass energy of 23.5 eV. In order to obtain the sp^2 fraction, the C 1s spectra were fitted to 3 Gaussian-Lorentzian peaks (C=C—C, 284.6 eV; C—O—C, 286.8 eV; and C=O/HO—C=O, 288.2 eV) using the constraint of equal Gaussian-Lorentzian prefactors, while leaving the full-width at half-maximum (fwhm) of the peaks to be freely variable. A similar fitting technique was used for the O 1s spectrum.

GO Functionalization and Cell-Capture Experiments. Coating of glass slides was performed by dip-coating in a solution of GO, and the immobilization of VHHs was performed using a click reaction (see Figure 2a) onto DBCO-modified⁵³ GO nanosheets. Briefly, GO-coated slides were initially activated with (1-ethyl-3-[3-(dimethylamino)propyl] carbodiimide) and *N*-hydroxysulfosuccinimide in 0.1 M MES buffer (2-[morpholino] ethanesulfonic acid, 0.5 M NaCl, pH = 6.0). Slides were washed and coupled with poly(ethylene glycol, $n = 12$) bis(amine) in PBS at 25 °C, followed by installation of dibenzocyclooctyne-sulfo-*N*-hydroxysuccinimide ester in PBS. Both *treated*- and *control*-GO substrate slides were assembled with another blocked glass slide to form a cell capture chamber.

Murine A20 cells were maintained in complete RPMI-1640 medium containing 10% inactivated fetal calf serum (IFS), 55 μM β -Mercaptoethanol, 1 mM sodium pyruvate and 1% penicillin/streptomycin (P/S). Different A20 cell concentrations were adjusted by diluting with PBS (from a starting concentration of 2×10^5 cells per 30 μL). The cell suspensions (total volume of 30 μL) were gently loaded into the functionalized capture chamber and incubated at room temperature for 10 min. After 3 \times PBS washes, the cells were fixed, washed with PBS and incubated with the anti-murine Class II MHC (I-A/I-E) Alexa 488-labeled antibody (Cat. #107616, Biolegend, CA, USA), in a 1:1000 dilution, for 1 h. at 25 °C. After washing, the captured cells were observed under fluorescence and confocal microscopy. In parallel, capture chambers without VHH7 loading (no functionalization), or

with VHH4 loading, served as the negative controls for the cell capture assays.

For cell capture from whole blood, fresh blood samples were obtained from Class II MHC-eGFP knock-in mice, and collected in heparin tubes (the concentration was determined to be 15,000 cells per 30 μL). The blood samples (total volume of 30 μL) were then loaded into the capture chamber at room temperature for 10 min. For quantitative analyses, the average number of captured cells was obtained by counting 10 representative micrographs from 3 independent cell capture device experiments.

Molecular Dynamics Simulations. MD simulations used to prepare realistic GO structures were carried out using the LAMMPS package⁵⁴ with the ReaxFF reactive force-field, chosen here for its ability to accurately describe bond-breaking and formation events in hydrocarbon systems.⁵⁵ We used 3×1.3 nm periodic graphene sheets with different oxidized and graphitic domain sizes, functionalized with randomly distributed epoxy and hydroxyl groups. The temperature of the GO sheets was increased from 10 to 300 K over a time interval of 250 fs. The system was then annealed at 300 K for 250 ps to allow for structural stabilization. A time step of 0.25 fs and the NVT Berendsen thermostat was employed in our simulations.

ASSOCIATED CONTENT

Supporting Information

The Supporting Information is available free of charge on the ACS Publications website at DOI: 10.1021/acsnano.6b06979.

Figures S1–S12; Tables S1–S3 (PDF)

AUTHOR INFORMATION

Corresponding Authors

*E-mail: jcg@mit.edu.

*E-mail: belcher@mit.edu.

*E-mail: guanyu@nctu.edu.tw.

ORCID

Neelkanth M. Bardhan: 0000-0002-4343-4007

Hidde L. Ploegh: 0000-0002-1090-6071

Present Address

[⊗]Optical Materials Engineering Laboratory, ETH Zurich, 8092 Zurich, Switzerland.

Author Contributions

[¶]N.M.B. and P.V.K. contributed equally to this work. N.M.B., P.V.K. and G.Y.C. conceived the idea and designed the experiments, with inputs from A.M.B., J.C.G., and H.L.P. Z.L. and G.Y.C. prepared the cell capture devices, with materials processing help from N.M.B. G.Y.C. performed the cell capture assays and the image analyses. P.V.K. performed the MD simulations and analyzed the results. N.M.B. performed the UV-vis and XPS analyses and correlated them with the simulation results. N.M.B. and P.V.K. cowrote the manuscript, with inputs from A.M.B., G.Y.C., H.L.P. and J.C.G.

Notes

The authors declare the following competing financial interest(s): Four of the authors, N.M.B., P.V.K., J.C.G. and A.M.B. declare financial interest, as Inventors listed on the US Patent #9,527,741 B2, and patent application PCT/US2014/036862, "Compositions Comprising Enhanced Graphene Oxide Structures and Related Methods".

ACKNOWLEDGMENTS

N.M.B. and A.M.B. would like to acknowledge the support of the Army Research Office Institute of Collaborative Biotechnologies (ICB) Grant #017251-022. P.V.K. and J.C.G. wish to thank financial support from the Tata Center and Solar Frontiers

Program at MIT, and the TACC Stampede system for computational resources. H.L.P. would like to acknowledge support from NIH (4DP1GM106409, R01AI87879). G.Y.C. would like to acknowledge financial support from National Chiao Tung University (105W970) and Ministry of Science and Technology (MOST 104-2314-B-009-001, MOST 105-2633-B-009-003), Taiwan.

REFERENCES

- (1) Allard, W. J.; Matera, J.; Miller, M. C.; Repollet, M.; Connelly, M. C.; Rao, C.; Tibbe, A. G. J.; Uhr, J. W.; Terstappen, L. W. M. M. Tumor Cells Circulate in the Peripheral Blood of All Major Carcinomas but not in Healthy Subjects or Patients with Nonmalignant Diseases. *Clin. Cancer Res.* **2004**, *10*, 6897–6904.
- (2) Bardhan, N. M.; Ghosh, D.; Belcher, A. M. Carbon Nanotubes as *in vivo* Bacterial Probes. *Nat. Commun.* **2014**, *5*, 4918.
- (3) Singh, S.; Upadhyay, M.; Sharma, J.; Gupta, S.; Vivekanandan, P.; Elangovan, R. A Portable Immunomagnetic Cell Capture System to Accelerate Culture Diagnosis of Bacterial Infections. *Analyst (Cambridge, U. K.)* **2016**, *141*, 3358–3366.
- (4) Smerage, J. B.; Barlow, W. E.; Hortobagyi, G. N.; Winer, E. P.; Leyland-Jones, B.; Srkalovic, G.; Tejwani, S.; Schott, A. F.; O'Rourke, M. A.; Lew, D. L.; et al. Circulating Tumor Cells and Response to Chemotherapy in Metastatic Breast Cancer: SWOG S0500. *J. Clin. Oncol.* **2014**, *32*, 3483–3489.
- (5) Liu, Z.; Tabakman, S.; Welsher, K.; Dai, H. Carbon Nanotubes in Biology and Medicine: *In vitro* and *in vivo* Detection, Imaging and Drug Delivery. *Nano Res.* **2009**, *2*, 85–120.
- (6) Xia, X.-R.; Monteiro-Riviere, N. A.; Riviere, J. E. An Index for Characterization of Nanomaterials in Biological Systems. *Nat. Nanotechnol.* **2010**, *5*, 671–675.
- (7) Yoon, H. J.; Kozminsky, M.; Nagrath, S. Emerging Role of Nanomaterials in Circulating Tumor Cell Isolation and Analysis. *ACS Nano* **2014**, *8*, 1995–2017.
- (8) Jung, J.; Cheon, D.; Liu, F.; Lee, K.; Seo, T. A Graphene Oxide Based Immuno-biosensor for Pathogen Detection. *Angew. Chem., Int. Ed.* **2010**, *49*, 5708–5711.
- (9) Wang, Y.; Li, Z.; Wang, J.; Li, J.; Lin, Y. Graphene and Graphene Oxide: Biofunctionalization and Applications in Biotechnology. *Trends Biotechnol.* **2011**, *29*, 205–212.
- (10) Chung, C.; Kim, Y.-K.; Shin, D.; Ryoo, S.-R.; Hong, B. H.; Min, D.-H. Biomedical Applications of Graphene and Graphene Oxide. *Acc. Chem. Res.* **2013**, *46*, 2211–2224.
- (11) Jariwala, D.; Sangwan, V. K.; Lauhon, L. J.; Marks, T. J.; Hersam, M. C. Carbon Nanomaterials for Electronics, Optoelectronics, Photovoltaics, and Sensing. *Chem. Soc. Rev.* **2013**, *42*, 2824–2860.
- (12) Stankovich, S.; Dikin, D. A.; Piner, R. D.; Kohlhaas, K. A.; Kleinhammes, A.; Jia, Y.; Wu, Y.; Nguyen, S. T.; Ruoff, R. S. Synthesis of Graphene-based Nanosheets *via* Chemical Reduction of Exfoliated Graphite Oxide. *Carbon* **2007**, *45*, 1558–1565.
- (13) Eda, G.; Fanchini, G.; Chhowalla, M. Large-Area Ultrathin Films of Reduced Graphene Oxide as a Transparent and Flexible Electronic Material. *Nat. Nanotechnol.* **2008**, *3*, 270–274.
- (14) Loh, K. P.; Bao, Q.; Eda, G.; Chhowalla, M. Graphene Oxide as a Chemically Tunable Platform for Optical Application. *Nat. Chem.* **2010**, *2*, 1015–1024.
- (15) Eda, G.; Chhowalla, M. Chemically Derived Graphene Oxide: Towards Large-Area Thin-Film Electronics and Optoelectronics. *Adv. Mater. (Weinheim, Ger.)* **2010**, *22*, 2392–2415.
- (16) Liu, Y.; Yu, D.; Zeng, C.; Miao, Z.; Dai, L. Biocompatible Graphene Oxide-Based Glucose Biosensors. *Langmuir* **2010**, *26*, 6158–6160.
- (17) Chen, G. Y.; Pang, D. W. P.; Hwang, S. M.; Tuan, H. Y.; Hu, Y. C. A Graphene-based Platform for Induced Pluripotent Stem Cells Culture and Differentiation. *Biomaterials* **2012**, *33*, 418–427.
- (18) Georgakilas, V.; Otyepka, M.; Bourlinos, A. B.; Chandra, V.; Kim, N.; Kemp, K. C.; Hobza, P.; Zboril, R.; Kim, K. S. Functionalization of Graphene: Covalent and Non-Covalent Approaches, Derivatives and Applications. *Chem. Rev. (Washington, DC, U. S.)* **2012**, *112*, 6156–6214.
- (19) Georgakilas, V.; Tiwari, J. N.; Kemp, K. C.; Perman, J. A.; Bourlinos, A. B.; Kim, K. S.; Zboril, R. Noncovalent Functionalization of Graphene and Graphene Oxide for Energy Materials, Biosensing, Catalytic, and Biomedical Applications. *Chem. Rev. (Washington, DC, U. S.)* **2016**, *116*, 5464–5519.
- (20) Dreyer, D. R.; Park, S.; Bielawski, C. W.; Ruoff, R. S. The Chemistry of Graphene Oxide. *Chem. Soc. Rev.* **2009**, *39*, 228–240.
- (21) Kannan, M. V.; Gnana kumar, G. Current Status, Key Challenges and its Solutions in the Design and Development of Graphene based ORR Catalysts for the Microbial Fuel Cell Applications. *Biosens. Bioelectron.* **2016**, *77*, 1208–1220.
- (22) Salamon, J.; Sathishkumar, Y.; Ramachandran, K.; Lee, Y. S.; Yoo, D. J.; Kim, A. R.; Gnana kumar, G. One-pot Synthesis of Magnetite Nanorods/Graphene Composites and its Catalytic Activity toward Electrochemical Detection of Dopamine. *Biosens. Bioelectron.* **2015**, *64*, 269–276.
- (23) Marcano, D. C.; Kosynkin, D. V.; Berlin, J. M.; Sinititskii, A.; Sun, Z.; Slesarev, A.; Alemany, L. B.; Lu, W.; Tour, J. M. Improved Synthesis of Graphene Oxide. *ACS Nano* **2010**, *4*, 4806–4814.
- (24) Yoon, H. J.; Kim, T. H.; Zhang, Z.; Azizi, E.; Pham, T. M.; Paoletti, C.; Lin, J.; Ramnath, N.; Wicha, M. S.; Hayes, D. F.; et al. Sensitive Capture of Circulating Tumor Cells by Functionalized Graphene Oxide Nanosheets. *Nat. Nanotechnol.* **2013**, *8*, 735–741.
- (25) Li, Y.; Lu, Q.; Liu, H.; Wang, J.; Zhang, P.; Liang, H.; Jiang, L.; Wang, S. Antibody-Modified Reduced Graphene Oxide Films with Extreme Sensitivity to Circulating Tumor Cells. *Adv. Mater. (Weinheim, Ger.)* **2015**, *27*, 6848–6854.
- (26) Yoon, H. J.; Shanker, A.; Wang, Y.; Kozminsky, M.; Jin, Q.; Palanisamy, N.; Burness, M. L.; Azizi, E.; Simeone, D. M.; Wicha, M. S.; et al. Tunable Thermal-Sensitive Polymer-Graphene Oxide Composite for Efficient Capture and Release of Viable Circulating Tumor Cells. *Adv. Mater. (Weinheim, Ger.)* **2016**, *28*, 4891–4897.
- (27) Perreault, F.; de Faria, A. F.; Nejati, S.; Elimelech, M. Antimicrobial Properties of Graphene Oxide Nanosheets: Why Size Matters. *ACS Nano* **2015**, *9*, 7226–7236.
- (28) Dave, S. H.; Gong, C.; Robertson, A. W.; Warner, J. H.; Grossman, J. C. Chemistry and Structure of Graphene Oxide via Direct Imaging. *ACS Nano* **2016**, *10*, 7515–7522.
- (29) Kappera, R.; Voiry, D.; Yalcin, S. E.; Branch, B.; Gupta, G.; Mohite, A. D.; Chhowalla, M. Phase-engineered Low-resistance Contacts for Ultrathin MoS₂ Transistors. *Nat. Mater.* **2014**, *13*, 1128–1134.
- (30) Acerce, M.; Voiry, D.; Chhowalla, M. Metallic 1T Phase MoS₂ Nanosheets as Supercapacitor Electrode Materials. *Nat. Nanotechnol.* **2015**, *10*, 313–318.
- (31) Kumar, P. V.; Bardhan, N. M.; Tongay, S.; Wu, J.; Belcher, A. M.; Grossman, J. C. Scalable Enhancement of Graphene Oxide Properties by Thermally driven Phase Transformation. *Nat. Chem.* **2014**, *6*, 151–158.
- (32) Zhang, M.; Wang, Y.; Huang, L.; Xu, Z.; Li, C.; Shi, G. Multifunctional Pristine Chemically Modified Graphene Films as Strong as Stainless Steel. *Adv. Mater. (Weinheim, Ger.)* **2015**, *27*, 6708–6713.
- (33) Liu, Q.; Zhang, M.; Huang, L.; Li, Y.; Chen, J.; Li, C.; Shi, G. High-Quality Graphene Ribbons Prepared from Graphene Oxide Hydrogels and Their Application for Strain Sensors. *ACS Nano* **2015**, *9*, 12320–12326.
- (34) Yamaguchi, H.; Ogawa, S.; Watanabe, D.; Hozumi, H.; Gao, Y.; Eda, G.; Mattevi, C.; Fujita, T.; Yoshigoe, A.; Ishizuka, S.; et al. Valence-band Electronic Structure Evolution of Graphene Oxide upon Thermal Annealing for Optoelectronics. *Phys. Status Solidi A* **2016**, *213*, 2380–2386.
- (35) Zhou, S.; Bongiorno, A. Origin of the Chemical and Kinetic Stability of Graphene Oxide. *Sci. Rep.* **2013**, *3*, 2484.
- (36) Chhowalla, M.; Ferrari, A. C.; Robertson, J.; Amaratunga, G. A. J. Evolution of sp² Bonding with Deposition Temperature in Tetrahedral Amorphous Carbon Studied by Raman Spectroscopy. *Appl. Phys. Lett.* **2000**, *76*, 1419–1421.

- (37) Ferrari, A. C.; Robertson, J. Interpretation of Raman Spectra of Disordered and Amorphous Carbon. *Phys. Rev. B: Condens. Matter Mater. Phys.* **2000**, *61*, 14095–14107.
- (38) Witte, M. D.; Cragolini, J. J.; Dougan, S. K.; Yoder, N. C.; Popp, M. W.; Ploegh, H. L. Preparation of Unnatural N-to-N and C-to-C Protein Fusions. *Proc. Natl. Acad. Sci. U. S. A.* **2012**, *109*, 11993–11998.
- (39) Chen, G.-Y.; Li, Z.; Theile, C. S.; Bardhan, N. M.; Kumar, P. V.; Duarte, J. N.; Maruyama, T.; Rashidfarrokhi, A.; Belcher, A. M.; Ploegh, H. L. Graphene Oxide Nanosheets Modified with Single-Domain Antibodies for Rapid and Efficient Capture of Cells. *Chem. - Eur. J.* **2015**, *21*, 17178–17183.
- (40) Kumar, P. V.; Bardhan, N. M.; Chen, G.-Y.; Li, Z.; Belcher, A. M.; Grossman, J. C. New Insights into the Thermal Reduction of Graphene Oxide: Impact of Oxygen Clustering. *Carbon* **2016**, *100*, 90–98.
- (41) Topsakal, M.; Ciraci, S. Domain Formation on Oxidized Graphene. *Phys. Rev. B: Condens. Matter Mater. Phys.* **2012**, *86*, 205402.
- (42) Huang, B.; Xiang, H.; Xu, Q.; Wei, S.-H. Overcoming the Phase Inhomogeneity in Chemically Functionalized Graphene: The Case of Graphene Oxides. *Phys. Rev. Lett.* **2013**, *110*, 085501.
- (43) Gao, W.; Alemany, L. B.; Ci, L.; Ajayan, P. M. New Insights into the Structure and Reduction of Graphite Oxide. *Nat. Chem.* **2009**, *1*, 403–408.
- (44) Bagri, A.; Mattevi, C.; Acik, M.; Chabal, Y. J.; Chhowalla, M.; Shenoy, V. B. Structural Evolution during the Reduction of Chemically Derived Graphene Oxide. *Nat. Chem.* **2010**, *2*, 581–587.
- (45) Kumar, P. V.; Bernardi, M.; Grossman, J. C. The Impact of Functionalization on the Stability, Work Function, and Photoluminescence of Reduced Graphene Oxide. *ACS Nano* **2013**, *7*, 1638–1645.
- (46) Kim, S.; Zhou, S.; Hu, Y.; Acik, M.; Chabal, Y. J.; Berger, C.; de Heer, W.; Bongiorno, A.; Riedo, E. Room-Temperature Metastability of Multilayer Graphene Oxide Films. *Nat. Mater.* **2012**, *11*, 544–549.
- (47) Sun, T.; Fabris, S.; Baroni, S. Surface Precursors and Reaction Mechanisms for the Thermal Reduction of Graphene Basal Surfaces Oxidized by Atomic Oxygen. *J. Phys. Chem. C* **2011**, *115*, 4730–4737.
- (48) Mattevi, C.; Eda, G.; Agnoli, S.; Miller, S.; Mkhoyan, K. A.; Celik, O.; Mastrogiorganni, D.; Granozzi, G.; Garfunkel, E.; Chhowalla, M. Evolution of Electrical, Chemical, and Structural Properties of Transparent and Conducting Chemically Derived Graphene Thin Films. *Adv. Funct. Mater.* **2009**, *19*, 2577–2583.
- (49) Carey, F. A. *Organic Chemistry*, 4th ed.; McGraw-Hill: Boston, 2000.
- (50) Reusch, W. Aldehydes & Ketones. 2013; <https://goo.gl/qQKCRB>, (accessed on Jan. 12, 2017).
- (51) Stankovich, S.; Piner, R. D.; Chen, X.; Wu, N.; Nguyen, S. T.; Ruoff, R. S. Stable Aqueous Dispersions of Graphitic Nanoplatelets via the Reduction of Exfoliated Graphite Oxide in the Presence of Poly(sodium 4-styrenesulfonate). *J. Mater. Chem.* **2006**, *16*, 155–158.
- (52) Park, S.; Hu, Y.; Hwang, J. O.; Lee, E.-S.; Casabianca, L. B.; Cai, W.; Potts, J. R.; Ha, H.-W.; Chen, S.; Oh, J.; et al. Chemical Structures of Hydrazine-treated Graphene Oxide and Generation of Aromatic Nitrogen Doping. *Nat. Commun.* **2012**, *3*, 638.
- (53) Li, Z.; Theile, C. S.; Chen, G.-Y.; Bilate, A. M.; Duarte, J. N.; Avalos, A. M.; Fang, T.; Barberena, R.; Sato, S.; Ploegh, H. L. Fluorophore-Conjugated Holliday Junctions for Generating Super-Bright Antibodies and Antibody Fragments. *Angew. Chem., Int. Ed.* **2015**, *54*, 11706–11710.
- (54) Plimpton, S. Fast Parallel Algorithms for Short-Range Molecular Dynamics. *J. Comput. Phys.* **1995**, *117*, 1–19.
- (55) van Duin, A. C. T.; Dasgupta, S.; Lorant, F.; Goddard, W. A. ReaxFF: A Reactive Force Field for Hydrocarbons. *J. Phys. Chem. A* **2001**, *105*, 9396–9409.